

This is a self-archived version of an original article. This version may differ from the original in pagination and typographic details.

Author(s): Luntinen, M.; Toivanen, V.; Koivisto, H.; Angot, J.; Thuillier, T.; Tarvainen, O.; Castro, G.

Title: Diagnostics of highly charged plasmas with multicomponent 1+ ion injection

Year: 2022

Version: Published version




Copyright: ©2022 American Physical Society

Rights: In Copyright

Rights url: <http://rightsstatements.org/page/InC/1.0/?language=en>

Please cite the original version:

Luntinen, M., Toivanen, V., Koivisto, H., Angot, J., Thuillier, T., Tarvainen, O., & Castro, G. (2022). Diagnostics of highly charged plasmas with multicomponent 1+ ion injection. *Physical Review E*, 106(5), Article 055208. <https://doi.org/10.1103/PhysRevE.106.055208>

Diagnostics of highly charged plasmas with multicomponent 1+ ion injectionM. Luntinen ^{*}, V. Toivanen , and H. Koivisto *Accelerator Laboratory, Department of Physics, University of Jyväskylä, FI-40014 Jyväskylä, Finland*J. Angot [†] and T. Thuillier *Univ. Grenoble Alpes, CNRS, Grenoble INP, LPSC-IN2P3, 38000 Grenoble, France*O. Tarvainen *UK Science and Technology Facilities Council, ISIS Pulsed Spallation Neutron and Muon Facility, Rutherford Appleton Laboratory, Harwell Campus, OX11 0QX, United Kingdom*G. Castro *INFN-LNS, Via S. Sofia 62, 95123, Catania, Italy*

(Received 21 June 2022; accepted 9 October 2022; published 16 November 2022)

We establish multicomponent 1+ injection into a charge breeder electron cyclotron resonance ion source and an associated computational procedure as a noninvasive probe of the electron density n_e , average electron energy $\langle E_e \rangle$, and the characteristic times of ionization, charge exchange, and ion confinement of stochastically heated, highly charged plasma. Multicomponent injection allows refining the n_e , $\langle E_e \rangle$ ranges, reducing experimental uncertainty. Na/K injection is presented as a demonstration. The $\langle E_e \rangle$ and n_e of a hydrogen discharge are found to be 600^{+600}_{-300} eV and $8^{+8}_{-3} \times 10^{11}$ cm⁻³, respectively. The ionization, charge exchange, and confinement times of high charge state alkali ions are on the order of 1 ms–10 ms.

DOI: [10.1103/PhysRevE.106.055208](https://doi.org/10.1103/PhysRevE.106.055208)**I. INTRODUCTION**

In past decades, the nuclear and astrophysics communities have migrated toward the use of radioactive ion beams (RIBs) for the study of nuclear structures far from stability [1]. The RIB production methods (e.g., the ISOL method [2]) generate low-intensity beams of singly charged, radioactive ions, which need to be postaccelerated to attain an energy required for nuclear physics experiments. The 1+ ions are usually further ionized before postacceleration in a process referred to as charge breeding [3,4].

In a charge breeder electron cyclotron resonance ion source (CB-ECRIS) [5] the radioactive 1+ species are injected at low energy and captured by the plasma, where the magnetically confined electrons are stochastically heated by microwave radiation. The electrons attain energies in the 10 eV to 100 keV range through resonant interaction with the microwave and are able to ionize the injected particles in a stepwise manner. The ionization is counteracted by charge exchange with the neutral atoms of the plasma, whereby the highly charged ion captures a valence electron from the neutral atom.

The electron impact ionization process is dominated by electrons at 10²–10³ eV energies. The high-energy electrons at 10⁴–10⁵ eV range are well confined and form a 3D dip in the positive ambipolar plasma potential profile [6,7], confin-

ing the highly charged ions. Consequently, the different ion populations form a nested layer structure, with higher charge states originating near the axis of the plasma chamber, and lower charge states from the peripheral plasma (see, e.g., simulations in Refs. [8,9]). The plasma loss processes (e.g., random-walk [10], ambipolar diffusion [11], rf scattering [12], and instabilities [13]) determine the rate at which ions escape confinement and become available for beam formation. The ion confinement time needs to be long compared to the ionization time for the ions to reach a high charge state. If the charge-bred species is radioactive, the confinement time must also be short compared to its half-life.

The charge-breeding process needs to be fast and efficient to enable the—usually quite low intensity—injecting radioactive 1+ ion beam to be charge bred to high charge states before radioactive decay causes significant losses. The ion production efficiency and breeding time must be understood to discern which radioactive isotopes are accessible for charge breeding and postacceleration, and to guide further development of the CB-ECRIS to access RIBs of short-lived isotopes. The total breeding time is relatively well understood phenomenologically [14] but the underlying physical causes have not yet been revealed by experiment. The diagnostic methods used to probe these properties must be noninvasive to avoid perturbing the tenuous plasma state. In effect, this constrains the methods to those usable in the same conditions as when delivering the RIB to the user.

We have recently developed a method which satisfies these conditions. The so-called consecutive transients (CT) method

^{*}miha.s.p.luntinen@jyu.fi[†]julien.angot@lpsc.in2p3.fr

[15,16] for estimating the ECR-heated plasma properties, i.e., the electron density, average energy of the EED, characteristic times of ionization, charge exchange, and ion confinement. It is based on causing a small perturbation and monitoring the response of the complex system to it, requiring fewer *a priori* assumptions than any previous method and, uniquely, accounts for the experimental uncertainty of the electron-impact ionization cross sections employed in the calculations involved in this and similar methods [17–21]. Stable alkali metal ions are used as a proxy for the true RIBs. Here we expound an experimental and computational methodology relying on multicomponent probing of the plasma. This allows physically constraining the results, circumventing the uncertainty of the ionization cross sections inherited by the CT method.

II. METHOD

The working principle of the CT method is as follows: A continuous beam of singly charged metallic ions is injected into the plasma of a CB-ECRIS from the 1+ ion source [22]. Metallic ions are chosen to prevent recirculation from the plasma chamber walls [23]. The operating parameters (neutral gas input rate, microwave heating power, magnetic mirror ratios, etc.) of the ECRIS are then optimized for the production of a desired charge state of the injected species in a process colloquially referred to as tuning.

Once the tune is established, the injected 1+ beam is pulsed by means of an electrostatic chopper to produce square 1+ ion pulses. It is important to minimize the perturbation on the plasma by selecting an appropriate pulse width (on the order of 10 ms) and injected 1+ current (~ 100 – 500 nA), limiting the rate of particles injected into the device to roughly two orders of magnitude less than the total rate of particles extracted from the plasma. It was shown in Ref. [15] that the modification of the high charge states' beam currents in the support plasma charge state distribution (CSD) was at most $\sim 5\%$ when injecting the 1+ species continuously at an intensity of 710 nA. The perturbation is even smaller in the pulsed injection mode with lower 1+ currents.

The temporal evolution of the volumetric density of charge state q in the plasma is described by the balance equation [7]

$$\begin{aligned} \frac{dn^q}{dt} = & + n_e \langle \sigma v \rangle_{q-1 \rightarrow q}^{\text{inz}} n^{q-1} - n_0 \langle \sigma v \rangle_{q \rightarrow q-1}^{\text{cx}} n^q \\ & + n_0 \langle \sigma v \rangle_{q+1 \rightarrow q}^{\text{cx}} n^{q+1} - n_e \langle \sigma v \rangle_{q \rightarrow q+1}^{\text{inz}} n^q \\ & - \frac{n^q}{\tau^q}, \end{aligned} \quad (1)$$

where $\langle \sigma v \rangle^{\text{inz/cx}}$ are the rate coefficients of ionization from the ground state and charge exchange (functions of the average energy of the electron or ion energy distribution, see Ref. [15]), n_0 , n^q , and n_e the neutral, ion, and electron densities, respectively. The final term $-n^q/\tau^q$ represents the rate of ion losses and defines the confinement time τ^q .

Since the injected beam is pulsed, the time series of the extracted beam is a transient whose shape is determined by Eq. (1). We measure the beam current time series (I^q) and fit

them with an equation derived from Eq. (1),

$$\frac{dI^q}{dt} = a_q I^{q-1} - b_q I^q + c_q I^{q+1}, \quad (2)$$

where the fit coefficients a_q , b_q , and c_q are functions of n_e and $\langle E_e \rangle$. At least five consecutive charge states' currents are required for the analysis.

Using an optimization procedure [15], it is possible to determine a range of n_e and $\langle E_e \rangle$ values consistent with the coefficients a_q , b_q , and c_q , and to calculate the characteristic times of ionization (from q to $q+1$) $\tau_{\text{inz}}^q = [n_e \langle \sigma v \rangle_{q \rightarrow q+1}^{\text{inz}}]^{-1}$, charge exchange (from q to $q-1$) $\tau_{\text{cx}}^q = [n_0 \langle \sigma v \rangle_{q \rightarrow q-1}^{\text{cx}}]^{-1}$, and ion confinement τ^q .

Similarly to the n_e and $\langle E_e \rangle$ values, a range of solutions is obtained for the characteristic times, and in lieu of additional constraints (e.g., the cutoff density [24] for n_e) the range may be very broad. There is evidence from both simulations and experiments that highly charged ions originate from the same plasma volume near the central axis of the plasma chamber [8,9,25–28] and, consequently, these ion populations probe the same plasma conditions, i.e., they have a common n_e $\langle E_e \rangle$ value. We may thus take the intersection of two or more solution sets of highly charged ion populations which constrains the results on the aforementioned physical basis. The intersection is obtained by multiplying the two-dimensional histograms generated from the distributions of the n_e , $\langle E_e \rangle$ points within the solution sets of the two populations.

The $\langle E_e \rangle$ dependence of the a_q , b_q , c_q coefficients arises via the rate coefficients, which are calculated under the assumption of a Maxwell-Boltzmann electron energy distribution (EED) for the warm electrons, since the actual EED is unknown. Experiments measuring the lost electron energy indicate a non-Maxwellian tail for the EED [29], but results with the kappa-distribution [30] have shown that the characteristic times obtained via the CT method are unaffected by even a large distortion of the shape of the EED.

There are three possibilities for applying the overlap-method: (i) overlap of different charge states of the same ion species (e.g., K^{9+} , K^{10+} , ...), (ii) overlap of the same charge states of different isotopes (e.g., $^{39}\text{K}^{9+}$ and $^{41}\text{K}^{9+}$), and (iii) overlap of high charge states of different ion species (e.g., K and Na). Each case is justified for HCIs for the reasons mentioned in the previous paragraph. Additionally, case (ii) is justified whenever the two isotopes' masses are similar enough not to cause a significant difference in their spatial distribution. We will focus on category (iii) as a sample case, since the different ionization cross sections of the two species help mitigate the effects of the large experimental uncertainty of the ionization cross sections currently available; data from Refs. [31,32] are used in this paper. Results for cases (i) and (ii) are presented in the Appendices alongside additional discussion.

A. Overlap analysis of Na and K

The data [33] were collected on the LPSC 14.5 GHz CB-ECRIS test bench [5,15] (see also Appendix A). The experimental setup was amended by loading the 1+ ion source

with a Na/K composite pellet, which enables producing a beam of Na^+ and K^+ and quickly switching between them by retuning the injection beam line, without having to adjust the CB-ECRIS parameters. Due to the internal uncertainties involved in tuning the CB-ECRIS, no-stop component switching is paramount to ensure that the same plasma conditions are probed by both injected species. The CB-ECRIS was tuned for Na^{8+} production, and pulsed beams of 100 nA and 200 nA of $^{23}\text{Na}^+$ and $^{39}\text{K}^+$, respectively, were injected in 10 ms pulses into the hydrogen discharge sustained in the source. The injection beamline optics were tuned for each injected 1+ species, and the extracted highly charged ion beam currents were measured at the N+ Faraday Cup, downstream of the CB-ECRIS (see Appendix A). The experimental parameters are tabulated in Table III in Appendix B.

The time series of the charge bred K and Na beam current transients (the N+ currents) were analyzed using the CT-analysis codes (the CT analyzer) [34] and the n_e , $\langle E_e \rangle$ postdictions consistent with the measured time series—and the corresponding characteristic times—were obtained. Each $(n_e, \langle E_e \rangle)$ pair of the solution set satisfies the fitting parameters a_q, b_q, c_q and is thus a possible value of the plasma density and average energy within the plasma volume whence the K and Na ions originate. On the order of 10^4 postdictions were obtained in each set. The $n_e, \langle E_e \rangle$ range where solutions were sought was limited on physical grounds. The density was constrained to the range $10^{11} \text{ cm}^{-3} < n_e < 2.6 \times 10^{12} \text{ cm}^{-3}$, where the upper limit is the cutoff density for 14.5 GHz microwaves and the lower limit is a conservative estimate based on results from Ref. [13]. 3D Monte Carlo simulations [35] suggest that the plasma within the ECR zone may be overdense (i.e., n_e greater than the cutoff density). However, there is no direct experimental evidence of this. The average energy of the EED was set to the range $10 \text{ eV} < \langle E_e \rangle < 10 \text{ keV}$, where the lower limit is the order of magnitude of the plasma potential [36] and the upper limit was chosen based on Ref. [11].

Based on simulation results for the spatial distribution of ions [9], it can be argued that ions having a charge state above the peak in the CSD can be said to originate from the same plasma volume. Figure 1 shows the CSD (continuous 1+ injection) of K and Na, which indicates that the peak occurs for Na^{6+} and K^{9+} . It was found that in the data set presented here, a mutual overlap of $(n_e, \langle E_e \rangle)$ can be found for the populations of K^{9+} , K^{10+} , and Na^{7+} .

To obtain the overlap set, a 2D histogram was generated out of each $(n_e, \langle E_e \rangle)$ solution set (with 200×200 bins). These histograms were then multiplied binwise by one another, and the product histogram was normalized to the maximum density of solutions within the set, i.e., the region which contributes most to the characteristic times calculated within the set. Finally, only those $(n_e, \langle E_e \rangle)$ pairs falling into the nonzero bins of the product set were kept out of the original solution sets. This constrains the set of viable solutions significantly, as demonstrated hereafter.

III. RESULTS

Figure 2 shows the outlines of the individual solution sets of K^{9+} , K^{10+} , and Na^{7+} in $(\langle E_e \rangle, n_e)$ space, restricted on the

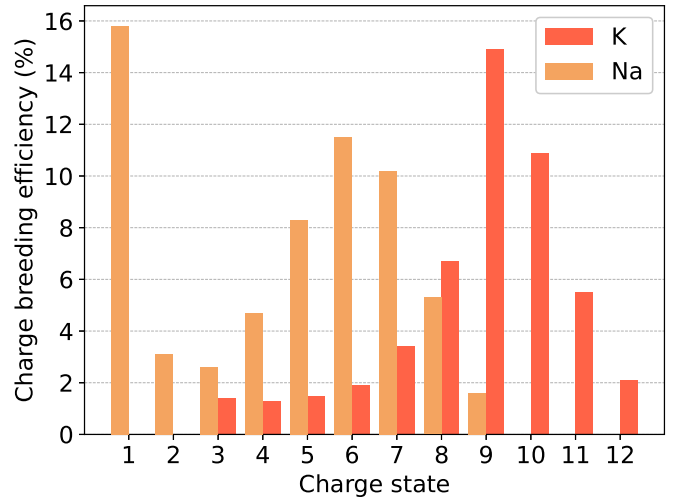


FIG. 1. Continuous mode charge breeding efficiencies of K and Na.

physical grounds discussed above, and Fig. 3 shows the heat map of their mutual overlap. The distributions of n_e and $\langle E_e \rangle$ values are projected as histograms on the margins of Fig. 3. To characterize the distributions, we tabulate the median value and in superscript and subscript we indicate the upper and lower confidence bounds, respectively, which enclose 34.1% of all solutions above and below the median. For example, the value $n_e = 4_{-3}^{+10} (10^{11} \text{ cm}^{-3})$ would describe a distribution whose median value is 4 (10^{11} cm^{-3}) and 68.2% of all n_e values would fall in the interval [1, 14] (10^{11} cm^{-3}). Figure 5 in Appendix C shows an example distribution obtained for the confinement time from the CT analyzer, with the median and the 34.1% bounds plotted as vertical lines.

Table I shows the median values of n_e and $\langle E_e \rangle$ as well as their 34.1% bounds for both the individual solution sets as well as the overlap. Similarly, Table II shows the median as well as the minimum characteristic times calculated from the individual solution sets, and within their mutual overlap. The

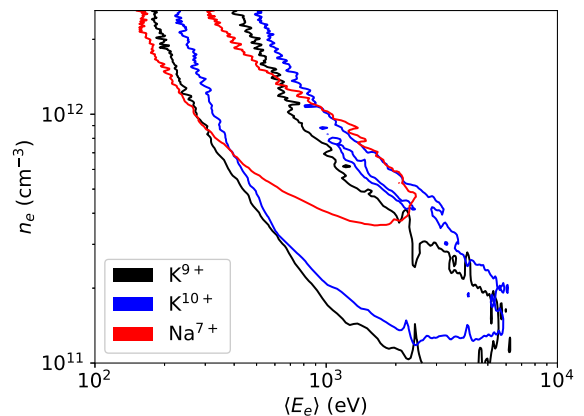


FIG. 2. The limits of the solution sets for K^{9+} , K^{10+} , and Na^{7+} . The threshold of the drawn contours has been set to 0.1 of the maximum density. The solution set ranges have been constrained based on physical considerations as described in the text. The image has been modified by an applied Gaussian filter for improved clarity.

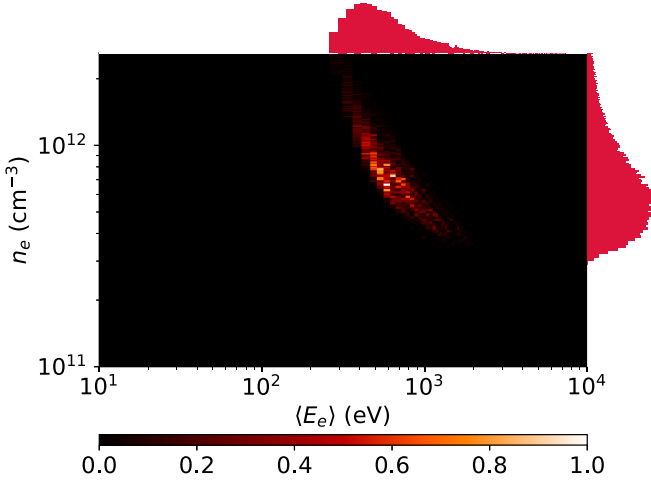


FIG. 3. Heat map of the overlap of the K^{9+} , K^{10+} , and Na^{7+} solution sets. Densities are normalized to the maximum density. Marginal histograms show the distribution of n_e and $\langle E_e \rangle$ values within the overlap set.

minimum values are tabulated for the characteristic times to highlight their order of magnitude in particular in the case of the confinement time.

We find that the uncertainty is reduced in almost all cases, and that in particular the n_e , and $\langle E_e \rangle$ distributions benefit from the overlap: For example, the median of $\langle E_e \rangle$ corresponding to the K^{10+} population decreases from 1300 eV to 600 eV, and the relative uncertainty from 200% to 150% when applying the overlap. The n_e median increases from $4 \times 10^{11} \text{ cm}^{-3}$ to $8 \times 10^{11} \text{ cm}^{-3}$, and the relative uncertainty decreases from 300% to 140%.

The characteristic time estimates are also generally improved, in particular the confinement times. The relative uncertainty of K^{10+} confinement time decreases from 140% to 100% with the overlap. Similar reduction in the error bars of the charge exchange times can be seen. We note also that the minimum confinement times are significantly longer than those suggested by Ref. [11].

IV. DISCUSSION

The CT method yields a postdiction for the range of electron densities and average energies (for the presumed EED), which can serve as a guide for plasma modeling. We have shown it to be possible to reduce the breadth of the n_e , $\langle E_e \rangle$ region by overlapping two or more solution sets—in partic-

TABLE I. Medians and 34.1% bounds of n_e and $\langle E_e \rangle$ calculated from the individual solution sets and within the overlap of K and Na. Applying the overlap (two-element injection) reduces the uncertainty.

	n_e (10^{11} cm^{-3})	$\langle E_e \rangle$ (eV)
K^{9+}	4^{+10}_{-3}	1000^{+1900}_{-600}
K^{10+}	4^{+9}_{-3}	1300^{+1800}_{-800}
Na^{7+}	7^{+6}_{-3}	900^{+4600}_{-500}
Overlap	8^{+8}_{-3}	600^{+600}_{-300}

TABLE II. The characteristic times of confinement, ionization, and charge exchange (τ^q , τ_{inz}^q , τ_{cx}^q , respectively) for K^{9+} , K^{10+} , and Na^{7+} within their mutual overlap and individually. The minimum value (Min.) of the distribution is given along with the median (Med.) and the upper and lower bounds enclosing 34.1% of solutions above and below the median. All data in units of ms.

	Ion	τ^q		τ_{inz}^q		τ_{cx}^q	
		Min.	Med.	Min.	Med.	Min.	Med.
Overlap	K^{9+}	5	8^{+6}_{-2}	2	3.5^{+5}_{-6}	3	16^{+14}_{-8}
	K^{10+}	8	16^{+11}_{-5}	4	7^{+2}_{-2}	4	9^{+4}_{-3}
	Na^{7+}	4	$5.3^{+1.7}_{-8}$	2	2.8^{+3}_{-4}	5	19^{+11}_{-8}
No overlap	K^{9+}	5	10^{+10}_{-4}	2	3.8^{+9}_{-7}	3	9^{+13}_{-5}
	K^{10+}	8	19^{+20}_{-7}	4	8^{+2}_{-2}	4	8^{+5}_{-3}
	Na^{7+}	4	$5.4^{+2.1}_{-9}$	2	2.8^{+3}_{-4}	5	20^{+11}_{-8}

ular, the overlap of two different species (K/Na) limits the range of solutions. This reduction in the n_e , $\langle E_e \rangle$ uncertainty is reflected to the characteristic times.

Of the three overlap methods (i)–(iii), the overlap of two isotopes of the same element [case (ii)] had next to no effect, as could be expected: Since the plasma properties were unchanged, with two-nucleon mass difference there shouldn't be large deviations between the solution sets. Overlapping multiple charge states of a given species, or multiple species [cases (i) and (iii)], led to noticeable decrease in the uncertainty. The overlap of two different species [case (iii)] has the added benefit that the different ionization cross sections (and their different experimental uncertainties) reduce the effect of the uncertainty of the cross section on the method results. The results for cases (i) and (ii) are presented in Appendices D and E.

In Ref. [15], it was shown that the CT-method can be used to identify bottlenecks in the charge breeding process; e.g., an electron shell closure inhibits the production of higher charge states, and must be compensated by a higher plasma energy content to decrease the ionization time. Multicomponent injection helps in identifying these bottlenecks by decreasing the possible range of $\langle E_e \rangle$ and n_e , which leads to decreased uncertainty of the characteristic time values.

The method precision is still limited by the uncertainty of the ionization cross sections, whose literature values carry in some cases an experimental uncertainty in excess of 100%. This uncertainty is partly inherited by the CT-method through the evaluation of the ionization rate coefficients. Arbitrarily curtailing the cross section uncertainty in the data analysis leads to a further reduction in the width of the distribution of the characteristic times, which motivates improving the cross-section data either experimentally or through modeling.

The confinement times found by means of the CT method support recent findings [37] where ion temperatures in ECR-heated plasma were found to be an order of magnitude higher than conventionally believed. Long confinement times—consistent with electrostatic confinement in a potential dip within the plasma potential profile—were hypothesized as a potential explanation. According to Table II, highly charged ions have a confinement time $\gtrsim 5$ ms.

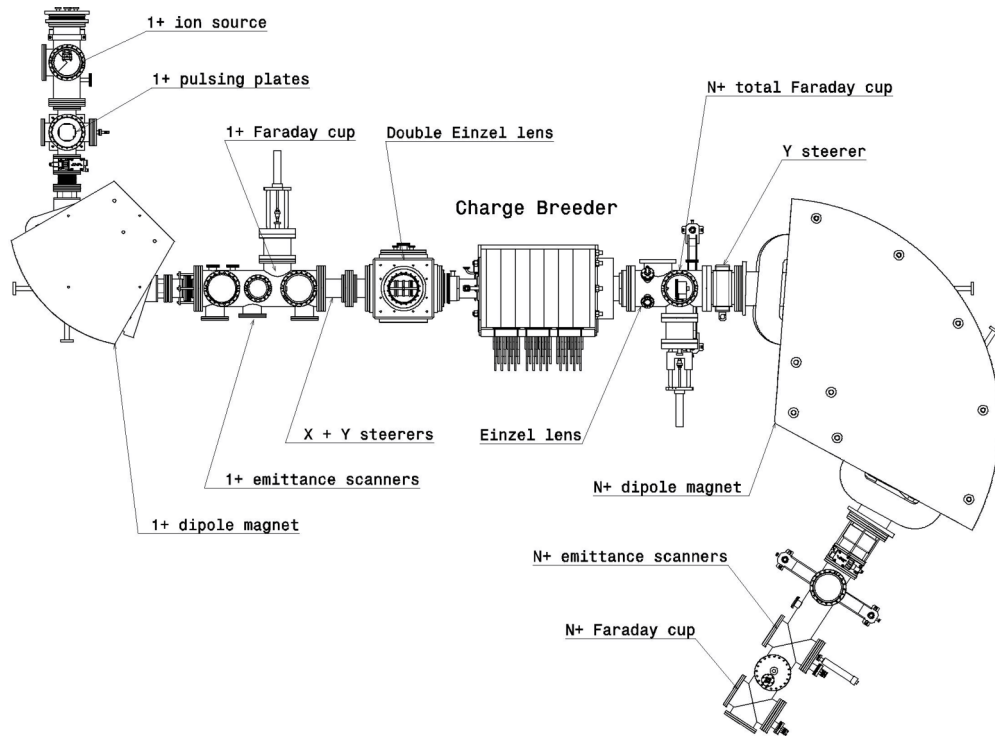


FIG. 4. Schematic layout of the 1+ → N+ PHOENIX-type 14.5 GHz CB-ECRIS test bench at LPSC.

Similarly long confinement time estimates have been found via other methods [19–21], with some simulations placing the total residence time of an ion inside the plasma at up to 100 ms [38]. The 100 ms residence time estimate is in agreement with the charge-breeding time measurements [14].

Reference [11] determined ion confinement times from the extracted beam currents via quasisimultaneous measurements of bremsstrahlung and $K\alpha$ emissions from the plasma, and found much shorter confinement times than those presented in this paper (at most <4 ms for Ar^{16+}) with a linear charge state dependence. However, their analysis may be influenced

by a circular reasoning as they fix the net ion density to obtain the EED from the bremsstrahlung emission, and later use the EED to compute the ion densities from the $K\alpha$ emissions. The linear dependency, and an assumption of 1 eV temperature for all ions, was used to conclude that the ambipolar diffusion model is the best candidate for ion confinement in an ECRIS. In Ref. [15], confinement times found via the CT method were shown to be best fitted by a power law rather than a linear fit. This and the charge state dependent ~ 10 eV ion temperatures found in Ref. [37] suggest ion confinement in the potential dip instead—the ions trapped in the dip would stay there until they attain the energy required to overcome the potential barrier $qe\Delta\phi$.

By solving Eq. (1) as a function of time, it is possible to obtain the plasma CSD, and from there one may estimate the intensity of extracted N+ ions. In the case of RIB production, one must amend Eq. (1) with a term describing loss rates to radioactive decay, allowing the estimation of extracted RIB intensity. Doing this requires knowledge of the characteristic times of stable proxy elements, for which the presented method provides improved information.

ACKNOWLEDGMENTS

We acknowledge grants of computer capacity from the Finnish Grid and Cloud Infrastructure [39] and support of the Academy of Finland Project funding (Grant No. 315855).

APPENDIX A: THE EXPERIMENTAL SETUP

The experimental campaign was conducted on the Laboratory of Subatomic Physics and Cosmology (LPSC) 1+ →

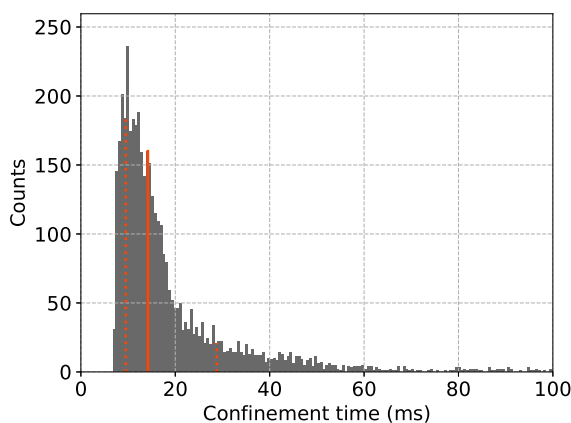


FIG. 5. The resultant confinement time distribution obtained for $^{41}\text{K}^{9+}$ in the helium discharge corresponding to the operating parameters of Table IV. The solid red line corresponds to the median and the dotted lines are the upper and lower bounds enclosing in total 68.2% of all results within the distribution.

TABLE III. ECRIS operating parameters for the Na/K overlap data set. The source was tuned for Na⁸⁺ production.

B _{inj}	1.54 T
B _{min}	0.45 T
B _{ext}	0.83 T
Microwave power	540 W (14.5 GHz)
Support gas species	H ₂
P _{inj}	11–12 (10 ⁻⁸ mbar)
P _{ext}	13–15 (10 ⁻⁸ mbar)
1+ pulse width	10 ms
³⁹ K ¹⁺ injection intensity	200 nA
²³ Na ¹⁺ injection intensity	100 nA
Extraction HV	20 kV

N+ test bench, schematically pictured in Fig. 4. Starting from the top left of the figure, the 1+ ion source, based on thermionic emission of positive ions from a heated sample, was used to produce the singly charged ions for injection into the charge breeder: the amount of injected material was controlled by adjusting the heating power on the pellet. The pulsing was achieved by the 1+ pulsing plates, which deflected the beam electrostatically. The 1+ dipole magnet was used to select the desired 1+ ion species based on the charge-to-mass ratio, and the 1+ Faraday cup enabled the precise measurement of the injected 1+ current. The PHOENIX-type 14.5 GHz CB-ECRIS was assembled with a hexapole providing a 0.8 T radial magnetic field strength at the plasma chamber wall, on the poles. The plasma electrode aperture size was 8 mm. After extraction from the ECRIS, the N+ dipole magnet allowed the selection of the charge-bred, highly charged ions based on their charge-to-mass ratio. The N+ Faraday cup was used to measure the transient time series of the N+ currents.

APPENDIX B: ECRIS OPERATING PARAMETERS

The CB-ECRIS operating parameters used in the campaign to produce the Na/K-overlap data set are tabulated in Table III. The operating parameters used in the campaign to produce the isotope overlap data set are tabulated in Table IV.

TABLE IV. Source operating parameters for the isotope overlap data set.

B _{inj}	1.52 T
B _{min}	0.41 T
B _{ext}	0.83 T
Microwave power	540 W (14.5 GHz)
Support gas species	He
P _{inj}	8–10 (10 ⁻⁸ mbar)
P _{ext}	9–15 (10 ⁻⁸ mbar)
1+ pulse width	10 ms
³⁹ K ¹⁺ injection intensity	270 nA
⁴¹ K ¹⁺ injection intensity	55 nA
Extraction HV	20 kV

TABLE V. The characteristic times of confinement, ionization, and charge exchange (τ^q , τ_{inz}^q , τ_{cx}^q , respectively) for ³⁹K⁹⁺ and ⁴¹K⁹⁺ within their mutual overlap, and individually. The minimum value of (Min.) of the distribution is given along with the median (Med.) and the upper and lower bounds enclosing 34.1% of solutions above and below the median. All data in units of ms.

	Ion	τ^q		τ_{inz}^q		τ_{cx}^q	
		Min.	Med.	Min.	Med.	Min.	Med.
Overlap	³⁹ K ⁹⁺	6	11 ⁺⁷ ₋₃	3	5.4 ⁺⁹ ₋₈	4	13 ⁺¹⁵ ₋₆
	⁴¹ K ⁹⁺	7	16 ⁺¹⁹ ₋₆	3	4.5 ⁺⁹ ₋₇	4	9 ⁺⁸ ₋₄
No overlap	³⁹ K ⁹⁺	6	13 ⁺¹² ₋₄	3	6 ⁺¹ ₋₁	4	10 ⁺¹² ₋₄
	⁴¹ K ⁹⁺	7	16 ⁺²⁰ ₋₆	3	4 ⁺¹ ₋₁	4	9 ⁺⁸ ₋₃

APPENDIX C: EXAMPLE CHARACTERISTIC TIME DISTRIBUTION

Figure 5 shows the confinement time values of ⁴¹K⁹⁺ individually using the ECRIS operating parameters tabulated in Table IV. The median value 14.2 ms is plotted in solid red, while the lower bound at 9.5 ms and the upper bound at 28.8 ms are plotted with dotted lines. The upper and lower bounds enclose 34.1% of the solutions above and below the median, respectively, i.e., the uncertainty is given with a confidence of 68.2%.

APPENDIX D: ISOTOPE OVERLAP

The potassium isotopes ³⁹K and ⁴¹K were selectively injected into the helium plasma of the charge breeder (the source operating parameters tabulated in Table IV). The resultant continuous injection mode CSDs are shown in Fig. 6. Although there is an apparent absolute difference in the charge breeding efficiencies of the two isotopes, it turns out that by multiplying the ³⁹K distribution by 1.16 yields the same shape as for ⁴¹K. We can thus be assured that the plasma properties are not markedly changed by the differing 1+ injection intensities: One expects more or less the same CSD for two

TABLE VI. The characteristic times of confinement, ionization, and charge exchange (τ^q , τ_{inz}^q , τ_{cx}^q , respectively) for ³⁹K¹⁰⁺ and ⁴¹K¹⁰⁺ within their mutual overlap, and individually. The minimum value of (Min.) of the distribution is given with the median (Med.) along with the upper and lower bounds enclosing 34.1% of solutions above and below the median. All data in units of ms.

	Ion	τ^q		τ_{inz}^q		τ_{cx}^q	
		Min.	Med.	Min.	Med.	Min.	Med.
Overlap	³⁹ K ¹⁰⁺	13	35 ⁺⁴³ ₋₁₄	4	5.8 ⁺⁹ ₋₉	6	11 ⁺⁶ ₋₃
	⁴¹ K ¹⁰⁺	10	18 ⁺¹² ₋₅	5	13 ⁺³ ₋₃	6	12 ⁺⁷ ₋₄
No overlap	³⁹ K ¹⁰⁺	13	36 ⁺⁴⁴ ₋₁₄	4	6 ⁺¹ ₋₁	6	11 ⁺⁶ ₋₃
	⁴¹ K ¹⁰⁺	10	18 ⁺¹⁵ ₋₅	5	13 ⁺⁴ ₋₃	5	12 ⁺⁸ ₋₄

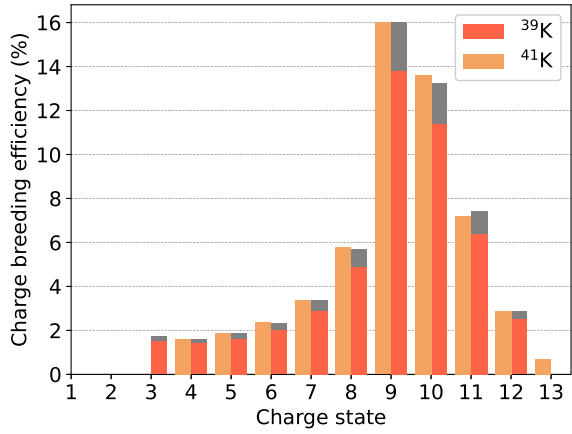
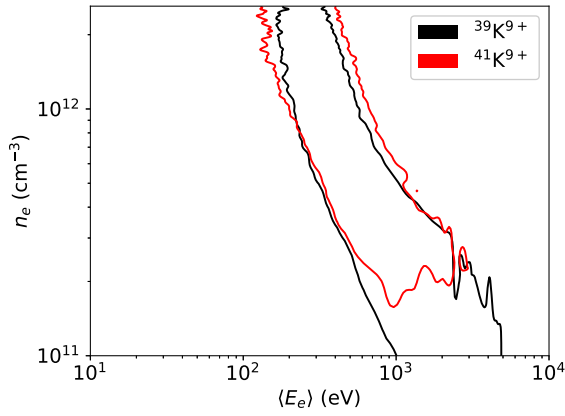
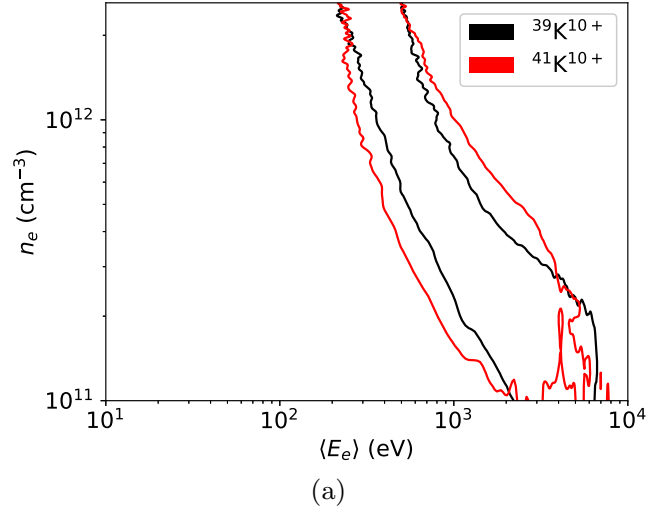
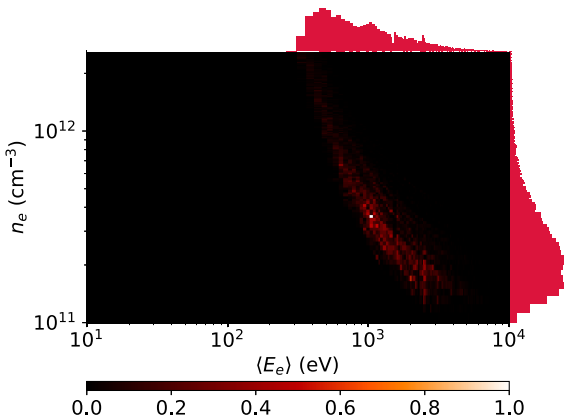


FIG. 6. The continuous mode charge breeding efficiencies of ^{39}K and ^{41}K . The gray bars represent the ^{39}K efficiency multiplied by 1.16, resulting in a distribution having the same shape as for ^{41}K .



(a)



(b) Overlap

FIG. 7. Outermost contours of the solution sets of $^{39}\text{K}^{9+}$ and $^{41}\text{K}^{9+}$ (a), and the heat map of their overlap (b). (a) has been modified by an applied Gaussian filter for clarity. The margin histograms show the distribution of n_e and $\langle E_e \rangle$ values within the solution set.

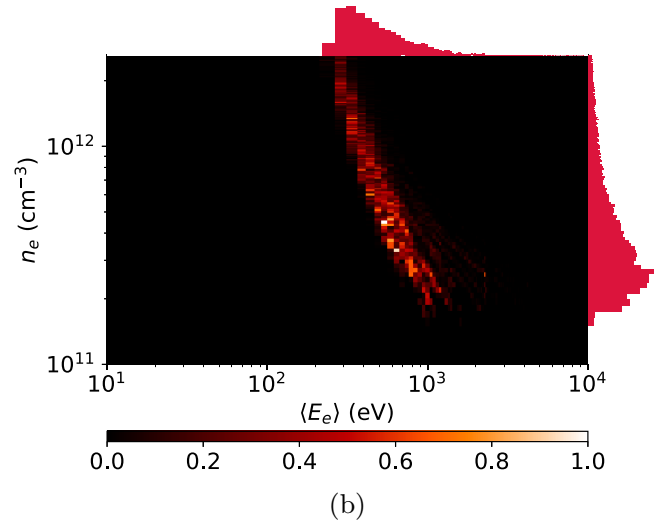


FIG. 8. Outermost contours of the solution sets of $^{39}\text{K}^{10+}$ and $^{41}\text{K}^{10+}$ (a) and the heat map of their overlap (b). (a) has been modified by an applied Gaussian filter for clarity. The margin histograms show the distribution of n_e and $\langle E_e \rangle$ values within the solution set.

isotopes of the same ion species if the plasma properties are unchanged, since they have the same electron configuration. Figures 7 and 8 present the solution sets of $^{39}\text{K}^{9+/10+}$ and $^{41}\text{K}^{9+/10+}$ and heat maps of their respective overlaps.

The characteristic time results for $^{39}\text{K}^{9+}$ and $^{41}\text{K}^{9+}$ are tabulated in Table V and the results for $^{39}\text{K}^{10+}$ and $^{41}\text{K}^{10+}$ in Table VI. The corresponding values for the obtained n_e , $\langle E_e \rangle$ distributions are found in Tables VII and VIII for the overlaps of $^{39/41}\text{K}^{9+}$ and $^{39/41}\text{K}^{10+}$, respectively.

APPENDIX E: CHARGE-STATE OVERLAP

Three different overlap sets of the high charge states of ^{41}K were taken: The charge states $^{41}\text{K}^{10+}$ – $^{41}\text{K}^{11+}$ were overlapped in set A, $^{41}\text{K}^{9+}$ – $^{41}\text{K}^{11+}$ in set B, and $^{41}\text{K}^{8+}$ – $^{41}\text{K}^{11+}$ in

TABLE VII. The electron densities n_e and averages energies of the EED $\langle E_e \rangle$ of the helium discharge obtained from $^{39}\text{K}^{9+}$ and $^{41}\text{K}^{9+}$ within their mutual overlap and individually. The median along with the upper and lower bounds enclosing 34.1% of solutions above and below the median is tabulated.

	n_e (10^{11}cm^{-3})	$\langle E_e \rangle$ (eV)
$^{39}\text{K}^{9+}$	$3.2^{+8.6}_{-1.7}$	890^{+1350}_{-520}
$^{41}\text{K}^{9+}$	$7.8^{+9.5}_{-4.6}$	510^{+580}_{-190}
Overlap	$5.9^{+9.9}_{-3.2}$	560^{+600}_{-230}

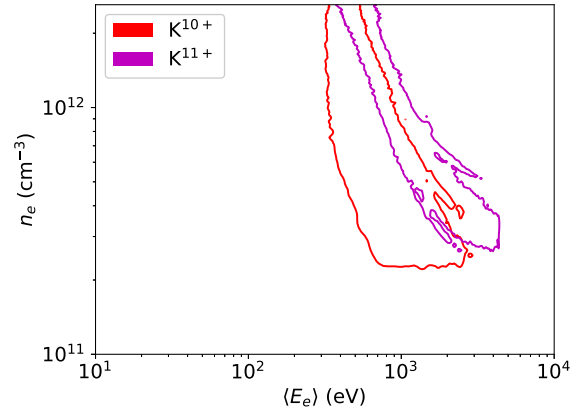
set C. The ECRIS operating parameters were the ones given in Table IV, and the CSD is the one shown in Fig. 6.

To obtain better statistics, the CT analyzer was run twice: First, the analysis was done as usual in the range $\langle E_e \rangle \in [10, 10000]$ eV, $n_e \in [1 \times 10^{11}, 2.6 \times 10^{12}] \text{cm}^{-3}$. The overlap was then taken, and the minimum and maximum $\langle E_e \rangle$ and n_e values common to each population in the set were selected as the new limits. The CT analyzer was then run with the new, constrained limits. The resultant contours of sets A, B, and C are presented in Fig. 9, and the estimates of n_e and $\langle E_e \rangle$ are presented in Table IX. The characteristic times computed within each of the overlaps are plotted in Fig. 10. We find that there is a reduction in the uncertainty when more charge states are overlapped. However, the uncertainty of the confinement time of $^{41}\text{K}^{9+}$ markedly increases when $^{41}\text{K}^{8+}$ is included in the overlap. This may indicate that $^{41}\text{K}^{8+}$ originates from a region of plasma with different plasma conditions, and we note that $^{41}\text{K}^{8+}$ is indeed below the CSD peak, and hence may correspond to a different plasma volume. In the case of the ionization time and the charge exchange time, inclusion of $^{41}\text{K}^{8+}$ leads to further reduction in the uncertainty.

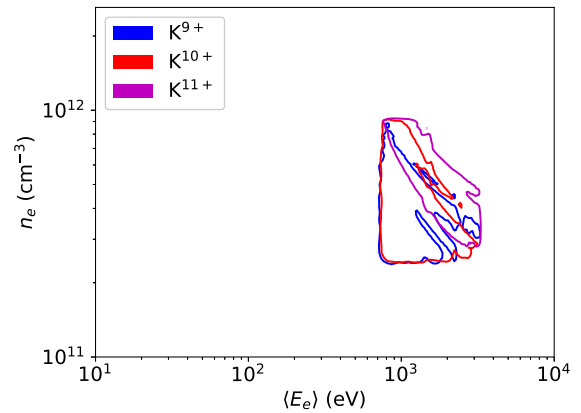
An interesting phenomenon in the ionization times emerges from the charge-state overlap: It appears that the ionization time of $^{41}\text{K}^{11+}$ is shorter than that of $^{41}\text{K}^{10+}$, which is unexpected considering that the ionization potential increases with charge state. We note that K^{11+} has three metastable excited states with lifetimes on the order of a few milliseconds, while K^{10+} only has one (see Table X). The greater number of metastable states could decrease the ionization time of K^{11+} compared to K^{10+} if the ionization occurs in a two-step process such that an electron first ionizes K^{11+} to a metastable

TABLE VIII. The electron densities n_e and averages energies of the EED $\langle E_e \rangle$ of the helium discharge obtained from $^{39}\text{K}^{10+}$ and $^{41}\text{K}^{10+}$ within their mutual overlap and individually. The median along with the upper and lower bounds enclosing 34.1% of solutions above and below the median is tabulated.

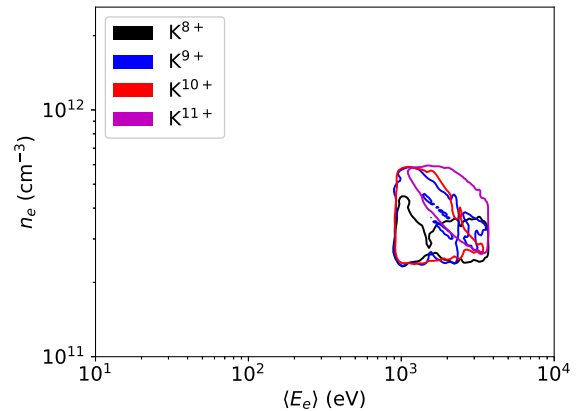
	n_e (10^{11}cm^{-3})	$\langle E_e \rangle$ (eV)
$^{39}\text{K}^{10+}$	$3.4^{+8.8}_{-1.7}$	1410^{+2240}_{-880}
$^{41}\text{K}^{10+}$	$4.1^{+7.5}_{-2.0}$	1240^{+1690}_{-690}
Overlap	$3.7^{+7.6}_{-1.8}$	1310^{+1760}_{-740}



(a)



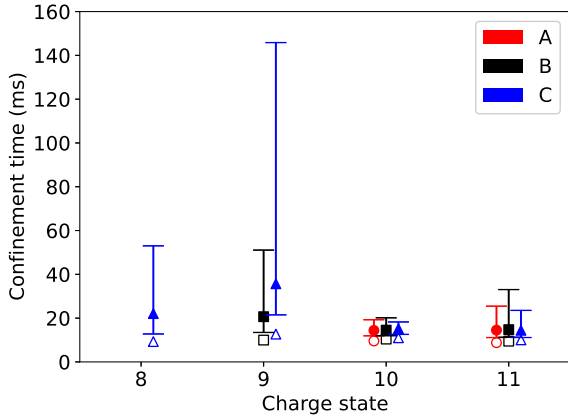
(b)



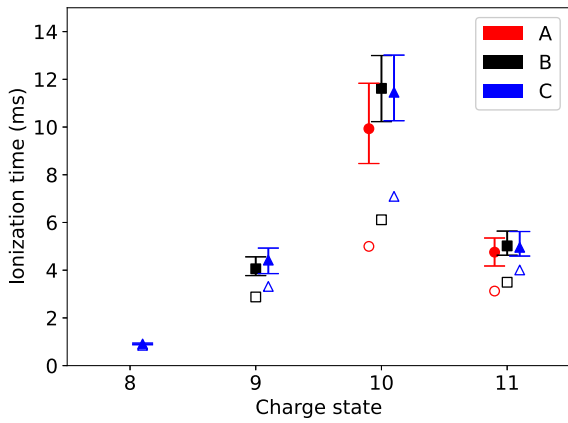
(c)

FIG. 9. The outermost contours of the solution sets for $^{41}\text{K}^{8+}$, $^{41}\text{K}^{9+}$, $^{41}\text{K}^{10+}$, and $^{41}\text{K}^{11+}$. Set A in (a), set B in (b), and set C in (c). The image has been modified by an applied Gaussian filter for improved clarity.

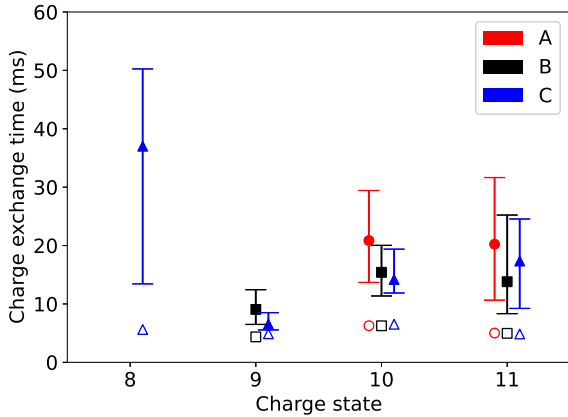
state, and a subsequent electron impact leads to ionization before the metastable state de-excites. This is, however, speculative, as possible processes leading to premature quenching of the metastable states are unknown.



(a)

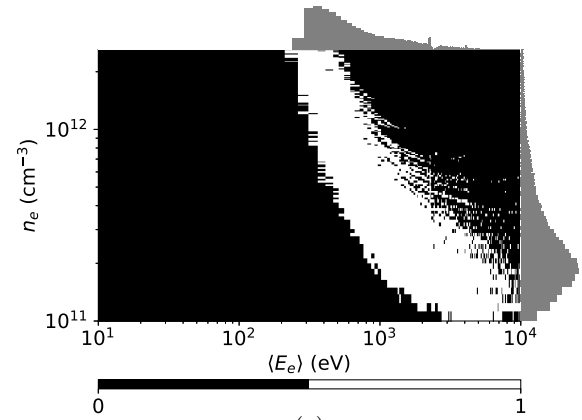


(b)

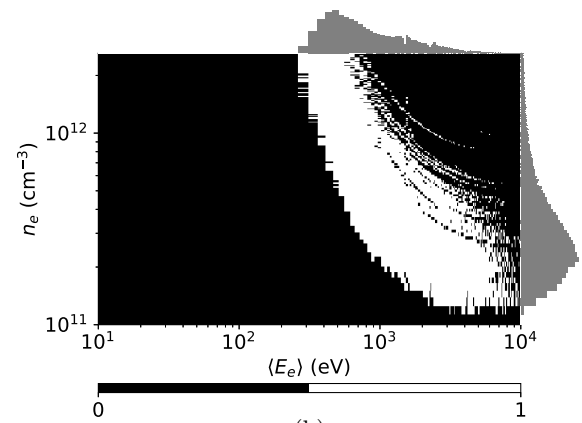


(c)

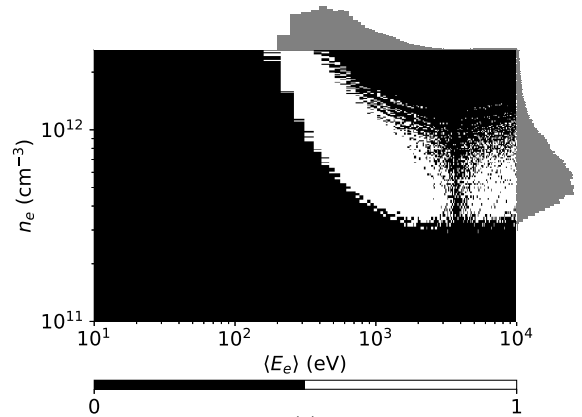
FIG. 10. The characteristic times of confinement (a), ionization (b), and charge exchange (c) obtained from the overlap sets of $^{41}\text{K}^{10+}$ – $^{41}\text{K}^{11+}$ (set A), $^{41}\text{K}^{9+}$ – $^{41}\text{K}^{11+}$ (set B), and $^{41}\text{K}^{8+}$ – $^{41}\text{K}^{11+}$ (set C). The median values of the distributions are plotted in solid markers, and the error bars enclose 34.1% of all solutions above and below the median. The minimum values are plotted by empty markers. The x -axis values have been slightly displaced for clarity.



(a)



(b)



(c)

FIG. 11. Binary heat map of the solution sets of K^{9+} (a), K^{10+} (b), and Na^{7+} (c). Margin histograms show the distribution of n_e and $\langle E_e \rangle$ values within the solution set.

APPENDIX F: SOLUTION SETS

Figure 11 shows two-dimensional histograms of the solution sets of $\text{K}^{9+/10+}$ and Na^{7+} obtained from the CT analysis code. The histogram plots have been generated with

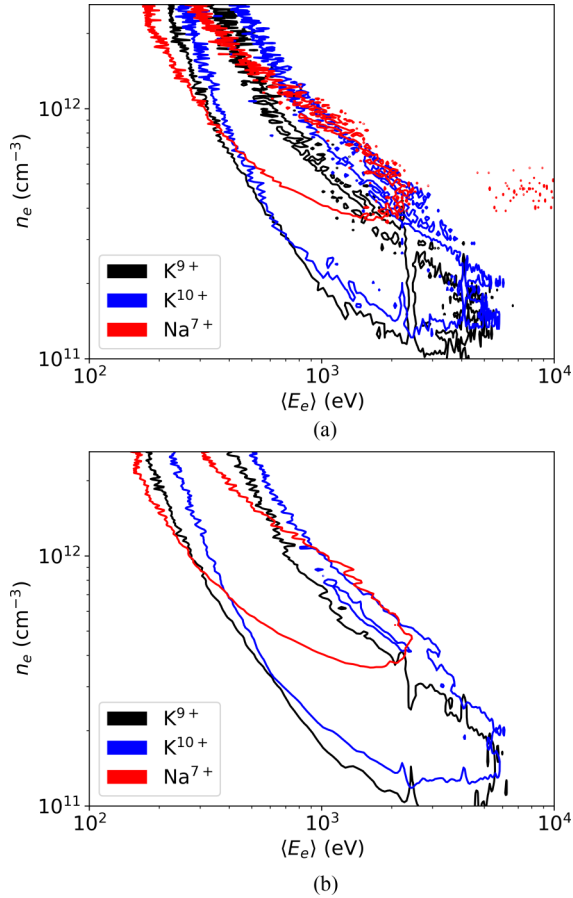


FIG. 12. Example of the effect of Gaussian filtering on the overlap contours. (a) has no applied Gaussian filter, while in (b) a Gaussian filtering with a standard deviation $\sigma = 1$.

200 \times 200 bins so if any solutions at all are found in a given bin, the histogram takes there the value 1. The distributions of the n_e and $\langle E_e \rangle$ values are plotted on the y and x margins, respectively.

APPENDIX G: GAUSSIAN FILTERING

Gaussian filtering is a classical method for removing noise from 2D photos and images, and its effect on our images

TABLE IX. The electron densities n_e and averages energies of the EED $\langle E_e \rangle$ obtained with different charge state overlaps of ^{41}K within their mutual overlap. The median along with the upper and lower bounds enclosing 34.1% of solutions above and below the median is tabulated.

Set	n_e (10^{11} cm^{-3})	$\langle E_e \rangle$ (eV)
A	$7.4^{+1.2}_{-3.5}$	1100^{+1300}_{-500}
B	$4.9^{+1.7}_{-1.2}$	1400^{+800}_{-400}
C	$3.6^{+0.9}_{-0.5}$	2400^{+700}_{-700}

TABLE X. Spontaneous metastable transitions of K^{10+} and K^{11+} [40,41].

Ion	Upper state	Lower state	Lifetime (ms)
K^{10+}	$2s^2 2p^5 \ ^2\text{P}^o_{1/2}$	$2s^2 2p^5 \ ^2\text{P}^o_{3/2}$	4.4
K^{11+}	$2s^2 2p^4 \ ^1\text{S}_0$	$2s^2 2p^4 \ ^3\text{P}_1$	0.2
	$2s^2 2p^4 \ ^1\text{D}_2$	$2s^2 2p^4 \ ^3\text{P}_2$	2.4
	$2s^2 2p^4 \ ^3\text{P}_1$	$2s^2 2p^4 \ ^3\text{P}_2$	6.7

is illustrated in Fig. 12. The filtering is done using the `gaussian_filter` function from Python's `scipy.ndimage` module, and its effect is to blur high-noise regions of the contour, which result from few non-zero regions outside of the general grouping. Without filtering, the contour is jagged, and applying the filter allows the reader to more easily see the general tendencies in the data. The effect is the same as when filtering noisy current signals in experimental measurements. We have taken great care to ensure that relevant portions of data are not obscured by the filtering—this is confirmed by eyeballing the produced images and adjusting the standard deviation σ of the Gaussian kernel accordingly. Only the contour images are affected by the filtering, and any (all) analysis of the overlap data sets is carried out using unfiltered data. The experimental data and codes required to reproduce the images in the paper are freely available and links to them are referenced within the paper. This includes all postprocessing routines such as plotting the contour images with or without the Gaussian filtering.

- [1] W. Gelletly, Radioactive ion beams: A new window on atomic nuclei, *Proc. Am. Philos. Soc.* **145**, 519 (2001).
- [2] M. Lindroos, Review of ISOL-type radioactive beam facilities, in *Proceedings of the EPAC'04* (JACoW Publishing, Geneva, Switzerland, 2004).
- [3] R. Geller, T. Lamy, and P. Sortais, Charge breeding of isotope on-line-created radioactive ions using an electron cyclotron resonance ion trap, *Rev. Sci. Instrum.* **77**, 03B107 (2006).
- [4] F. J. C. Wenander, Charge breeding of radioactive ions, edited by R. Bailey, [arXiv:1404.0945](https://arxiv.org/abs/1404.0945).

- [5] J. Angot, A. Galatá, L. Maunoury, T. Thuillier, M. Baylac, M. Migliore, P. Sole (LNL LPSC GANIL Collaboration), Contaminants reduction in ECR charge breeders, in *Proceedings of ECRIS 2020* (JACoW Publishing, MI, USA, 2020).
- [6] G. Melin, F. Bourg, P. Briand, J. Debernardi, M. Delaunay, R. Geller, B. Jacquot, P. Ludwig, T. K. N'Guyen, L. Pin, M. Pontonnier, J. C. Rocco, and F. Zadworny, Some particular aspects of the physics of the ECR sources for multicharged ions, *Rev. Sci. Instrum.* **61**, 236 (1990).
- [7] G. Shirkov, A classical model of ion confinement and losses in ECR ion sources, *Plasma Sources Sci. Technol.* **2**, 250 (1993).

- [8] V. Mironov and J. P. Beijers, Three-dimensional simulations of ion dynamics in the plasma of an electron cyclotron resonance ion source, *Phys. Rev. ST Accel. Beams* **12**, 073501 (2009).
- [9] V. Mironov, S. Bogomolov, A. Bondarchenko, A. Efremov, and V. Loginov, Numerical model of electron cyclotron resonance ion source, *Phys. Rev. ST Accel. Beams* **18**, 123401 (2015).
- [10] G. Melin, A. G. Drentje, A. Girard, and D. Hitz, Ion behavior and gas mixing in electron cyclotron resonance plasmas as sources of highly charged ions, *J. Appl. Phys.* **86**, 4772 (1999).
- [11] G. Douysset, H. Khodja, A. Girard, and J. P. Briand, Highly charged ion densities and ion confinement properties in an electron-cyclotron-resonance ion source, *Phys. Rev. E* **61**, 3015 (2000).
- [12] M. Sakildien, O. Tarvainen, R. Kronholm, I. Izotov, V. Skalyga, T. Kalvas, P. Jones, and H. Koivisto, Experimental evidence on microwave induced electron losses from ECRIS plasma, *Phys. Plasmas* **25**, 062502 (2018).
- [13] O. Tarvainen, T. Kalvas, H. Koivisto, J. Komppula, R. Kronholm, J. Laulainen, I. Izotov, D. Mansfeld, V. Skalyga, V. Toivanen, and G. Machicoane, Limitation of the ECRIS performance by kinetic plasma instabilities (invited), *Rev. Sci. Instrum.* **87**, 02A703 (2016).
- [14] J. Angot, O. Tarvainen, T. Thuillier, M. Baylac, T. Lamy, P. Sole, and J. Jacob, Charge breeding time investigations of electron cyclotron resonance charge breeders, *Phys. Rev. Accel. Beams* **21**, 104801 (2018).
- [15] J. Angot, M. Luntinen, T. Kalvas, H. Koivisto, R. Kronholm, L. Maunoury, O. Tarvainen, T. Thuillier, and V. Toivanen, Method for estimating charge breeder ECR ion source plasma parameters with short pulse 1+ injection of metal ions, *Plasma Sources Sci. Technol.* **30**, (2021).
- [16] M. Luntinen, J. Angot, O. Tarvainen, V. Toivanen, T. Thuillier, and H. Koivisto, Measurement of ionization, charge exchange and ion confinement times in charge breeder ECR ion sources with short pulse 1+ injection of metal ions, *J. Phys.: Conf. Ser.* **2244**, 012009 (2022).
- [17] R. C. Pardo, R. Harkewicz, and P. J. Billquist, Time evolution of charge states in an electron cyclotron resonance ion source, *Rev. Sci. Instrum.* **67**, 1602 (1996).
- [18] M. Imanaka, T. Nakagawa, H. Arai, I. Arai, and S. M. Lee, Plasma diagnostics of liquid He-free SC-ECR ion source (SHIVA) with use of laser ablation technique, *Nucl. Instrum. Methods Phys. Res., Sect. B* **237**, 647 (2005).
- [19] D. E. Neben *et al.*, Fast sputtering measurement studies using uranium with the NSCL ECR ion sources, in *Proceedings of ECRIS'16* (JACoW Publishing, Busan, Korea, 2016), pp. 128–132.
- [20] D. E. Neben, G. Machicoane, A. N. Pham, J. W. Stetson, G. Parsey, and J. P. Verboncoeur, An analysis of fast sputtering studies for ion confinement time, in *Proceedings of LINAC'16* (JACoW Publishing, MI, USA, 2016), pp. 475–477.
- [21] M. Marttinen, J. Angot, A. Annaluru, P. Jardin, T. Kalvas, H. Koivisto, S. Kosonen, R. Kronholm, L. Maunoury, O. Tarvainen, V. Toivanen, and P. Ujic, Estimating ion confinement times from beam current transients in conventional and charge breeder ECRIS, *Rev. Sci. Instrum.* **91**, 013304 (2020).
- [22] T. Lamy *et al.*, Experimental activities with the LPSC charge breeder in the European context, in *Proceedings of ECRIS'14* (JACoW Publishing, Geneva, Switzerland, 2014), pp. 120–126.
- [23] R. Geller, P. Ludwig, and G. Melin, Metal ion production in ECRIS (invited), *Rev. Sci. Instrum.* **63**, 2795 (1992).
- [24] R. Geller, *Electron Cyclotron Resonance Ion Sources and ECR Plasmas* (Institute of Physics Publishing, Bristol and Philadelphia, 1996).
- [25] S. Biri, A. Valek, T. Suta, E. Takcs, C. Szab, L. T. Hudson, B. Radics, J. Imrek, B. Juhsz, and J. Plinks, Imaging of ECR plasmas with a pinhole x-ray camera, *Rev. Sci. Instrum.* **75**, 1420 (2004).
- [26] L. Panitzsch, T. Peleikis, M. Stalder, and R. F. Wimmer-Schweingruber, Spatially resolved charge-state and current-density distributions at the extraction of an electron cyclotron resonance ion source, *Rev. Sci. Instrum.* **82**, 093302 (2011).
- [27] L. Panitzsch, T. Peleikis, M. Stalder, and R. F. Wimmer-Schweingruber, Experimental results: Charge-state and current-density distribution at the plasma electrode of an ECR ion source, in *Proceedings of ECRIS'12* (JACoW Publishing, Sydney, Australia, 2012), pp. 101–105.
- [28] R. Vondrasek, Diagnostics for multiple frequency heating and investigation of underlying processes, *Rev. Sci. Instrum.* **93**, 031501 (2022).
- [29] I. Izotov, O. Tarvainen, V. Skalyga, D. Mansfeld, T. Kalvas, H. Koivisto, and R. Kronholm, Measurement of the energy distribution of electrons escaping minimum-B ECR plasmas, *Plasma Sources Sci. Technol.* **27**, 025012 (2018).
- [30] V. Pierrard and M. Lazar, Kappa distributions: Theory and applications in space plasmas, *Sol. Phys.* **267**, 153 (2010).
- [31] K. L. Bell, H. B. Gilbody, J. G. Hughes, A. E. Kingston, and F. J. Smith, Recommended data on the electron impact ionization of light atoms and ions, *J. Phys. Chem.* **12**, 891 (1983).
- [32] M. A. Lennon, K. L. Bell, H. B. Gilbody, J. G. Hughes, A. E. Kingston, M. J. Murray, and F. J. Smith, Recommended data on the electron impact ionization of atoms and ions: Fluorine to nickel, *J. Phys. Chem. Ref. Data* **17**, 1285 (1988).
- [33] The experimental data are openly available at <https://doi.org/10.6084/m9.figshare.20071925>.
- [34] CT-analyzer release ct-analyzer-v2.0. Openly available at <https://github.com/misapema-jyfl/ct-analyzer>.
- [35] D. Mascali, S. Gammino, L. Celona, and G. Ciavola, Towards a better comprehension of plasma formation and heating in high performances electron cyclotron resonance ion sources (invited), *Rev. Sci. Instrum.* **83**, 02A336 (2012).
- [36] O. Tarvainen, P. Suominen, and H. Koivisto, A new plasma potential measurement instrument for plasma ion sources, *Rev. Sci. Instrum.* **75**, 3138 (2004).
- [37] R. Kronholm, T. Kalvas, H. Koivisto, J. Laulainen, M. Marttinen, M. Sakildien, and O. Tarvainen, Spectroscopic study of ion temperature in minimum-B ECRIS plasma, *Plasma Sources Sci. Technol.* **28**, 075006 (2019).
- [38] D. Mascali, L. Neri, L. Celona, G. Castro, G. Torrisi, S. Gammino, G. Sorbello, and G. Ciavola, A double-layer based model of ion confinement in electron cyclotron resonance ion source, *Rev. Sci. Instrum.* **85**, (2014).

- [39] Persistent identifier urn:nbn:fi:research-infras-2016072533.
- [40] A. Kramida, Yu. Ralchenko, J. Reader, and NIST ASD Team, NIST Atomic Spectra Database (Ver. 5.9), <https://physics.nist.gov/asd> (accessed June 17, 2022), National Institute of Standards and Technology, Gaithersburg, MD, 2021.
- [41] A. Kramida, Yu. Ralchenko, J. Reader, and NIST ASD Team, NIST Atomic Spectra Database (Ver. 5.9), <https://physics.nist.gov/asd> (accessed June 17, 2022), National Institute of Standards and Technology, Gaithersburg, MD, 2021.